

1 **Cryogenic silicification of microorganisms in hydrothermal fluids**

2 Mark G. Fox-Powell^{1,2}, Alan Channing³, Daniel Applin⁴, Ed Cloutis⁴, Louisa J. Preston⁵ & Claire R.
3 Cousins*^{1,2}

4 ¹*School of Earth and Environmental Sciences, University of St Andrews, Irvine Building, North Street, St*
5 *Andrews, Fife, UK, KY16 9AL.*

6 ²*St Andrews Centre for Exoplanet Science, University of St. Andrews, UK*

7 ³*School of Earth and Ocean Sciences, Cardiff University, Cardiff, Wales, UK, CF10 3AT.*

8 ⁴*Department of Geography, University of Winnipeg, Winnipeg, MB, Canada R3B 2E9.*

9 ⁵*Department of Earth and Planetary Science, Birkbeck, University of London, Malet St., Bloomsbury,*
10 *London, UK*

11 *Corresponding author: crc9@st-andrews.ac.uk

12

13 **ABSTRACT**

14 **Silica-rich hydrothermal fluids that experience freezing temperatures precipitate cryogenic opal-A**
15 **(COA) within ice-bound brine channels. We investigated cryogenic silicification as a novel**
16 **preservation pathway for chemo- and photo-lithotrophic Bacteria and Archaea. We find that the co-**
17 **partitioning of microbial cells and silica into brine channels causes microorganisms to become**
18 **fossilised in COA. Rod- and coccoidal-form Bacteria and Archaea produce numerous cell casts on**
19 **COA particle surfaces, while *Chloroflexus* filaments are preserved inside particle interiors. COA**
20 **particles precipitated from natural Icelandic hot spring fluids possess similar biomorphic casts,**
21 **including those containing intact microbial cells. Biomolecules and inorganic metabolic products are**
22 **also captured by COA precipitation, and are detectable with a combination of visible - shortwave**

23 **infrared reflectance, FTIR, and Raman spectroscopy. We identify cryogenic silicification as a newly**
24 **described mechanism by which microbial biosignatures can be preserved within silica-rich**
25 **hydrothermal environments. This work has implications for the interpretation of biosignatures in**
26 **relic hydrothermal settings, and for life-detection on Mars and Enceladus, where opaline silica**
27 **indicative of hydrothermal activity has been detected, and freezing surface conditions predominate.**

28 **KEYWORDS:** Cryogenic Opal-A; silicification; microfossils; biosignatures; hydrothermal

29

30 1. INTRODUCTION

31 Opaline silica (opal-A) has been a common preservation agent for microorganisms throughout the Earth's
32 geological record^{1,2}, and is found in many neutral-alkaline hydrothermal systems worldwide. Precipitated
33 by the cooling of aqueous hydrothermal solutions, colloidal silica is widely observed to mineralise
34 microbial cells^{1,3} and mats, and associated organic material⁴ in modern-day siliceous hot spring
35 environments. Ambient temperature groundwater springs are also capable of precipitating silica and
36 entombing microbes, preserving them as microfossils⁵, and relic Archaean hot spring silica sinters may
37 preserve some of the oldest evidence for life on Earth⁶. This physical capturing and subsequent silicification
38 of microbial biosignatures makes opaline silica an attractive target material in the search for life beyond
39 Earth, namely on Mars, and icy moons (i.e. Europa and Enceladus)^{2,7}.

40 Opal-A has been observed on Mars⁸⁻¹¹ in association with volcanic centres¹⁰ and hydrovolcanic structures¹²,
41 while one of the shortlisted landing sites for the NASA Mars 2020 rover includes a relic hydrothermal
42 system bearing opal-A deposits^{9,13}. Recent detections of colloidal silica associated with Enceladus¹⁴, and
43 molecular hydrogen within the Enceladan cryovolcanic plumes¹⁵ offer the strongest evidence to date for
44 ongoing hydrothermal activity on another planetary body, and suggests that the liquid water sourcing these
45 plumes has conditions suitable for biological methanogenesis^{15,16}. The sub-freezing surface temperatures
46 that have prevailed on Mars for much of its history¹⁷, and characterise present-day conditions on icy moons,

47 mean that silicification mechanisms will differ from those typically observed on Earth. This has direct
48 implications for the preservation of any resident microorganisms and their biosignatures.

49 Under non-freezing conditions, silica-chloride hot springs precipitate siliceous sinters through the cooling
50 of hot (>100 °C) silica-supersaturated hydrothermal fluids, which leads to the nucleation and eventual
51 sedimentation of colloidal silica. When warm hydrothermal fluids are discharged into a freezing
52 environment, the crystallisation of water as ice accelerates the precipitation of colloidal silica, which is
53 forced into brine veins in between ice crystals, along with dissolved solutes (such as Na⁺ and Cl⁻)¹⁸. The
54 result is the precipitation of cryogenic opal-A (COA) particles with distinctive morphologies defined by the
55 physical dimensions within the brine veins¹⁸. Microorganisms are known to partition into brine vein
56 networks in ice, exploiting them as a liquid water microenvironment¹⁹. However, the fate of
57 microorganisms when opal-A precipitates within these brine channels has not been previously investigated.
58 Terrestrial environments where both silica and microorganisms can be co-partitioned during ice formation
59 are found in geothermal regions in Iceland and Yellowstone National Park (USA) where the air temperature
60 is seasonally sub-zero °C for >50% of the year^{18,20}, and in high altitude geothermal systems such as El Tatio
61 (Chile)²¹. Silicified microorganisms associated spatially with COA particles from Iceland have been
62 previously observed³, however without any prior demonstration of silicification under cryogenic conditions,
63 it is not possible to ascertain whether they formed cryogenically or during subsequent mineralisation under
64 non-freezing conditions. Here, we combine an examination of natural COA samples from Iceland with
65 experimental cyrosilicification of microorganisms to investigate the preservation (or lack thereof) for
66 microorganisms and associated spectral biosignatures during freezing of silica-rich hydrothermal fluids.

67

68

69

70

71 **2. MATERIALS AND METHODS**

72 **2.1. Microbial strains and growth conditions**

73 Four previously described microbial strains were selected to experimentally test the process of microbial
74 cryosilicification. The strains were chosen primarily to capture a range of morphological, metabolic and
75 phylogenetic diversity representative of microorganisms found across a diverse range of hydrothermal
76 systems²²⁻²⁴, with an emphasis on readily-cultivable strains isolated from high-temperature neutral-alkaline
77 environments. Where possible, strains isolated from hydrothermal systems were used. Strains included (i)
78 the thermophilic sulfate-reducing bacterium *Thermodesulfovibrio islandicus* DSMZ-12570²⁵, (ii) the
79 thermophilic methanogenic archaeon *Methanoculleus thermophilus* DSMZ-2373²⁶, (iii) the filamentous
80 anoxygenic phototroph *Chloroflexus aurantiacus* DSMZ-635²⁷, and (iv) the photoferrotrophic bacterium
81 *Rhodopseudomonas palustris* TIE-1²⁸. *R. palustris* grows readily with either Fe²⁺ or acetate as an electron
82 donor for phototrophy, thus batches cultivated on both substrates were used in experiments to assess
83 differences in silicification and resulting biosignatures for these different metabolic pathways. Growth
84 media and conditions were all as described previously²⁵⁻²⁸, with the exception of *C. aurantiacus*, which was
85 cultivated under natural daylight in a clear-fronted incubator rather than under the recommended 1000 lux.
86 This resulted in slower growth but no discernible difference to cellular morphology.

87

88 **2.2. Experimental silicification**

89 Sodium metasilicate (Na₂SiO₃·5H₂O) was dissolved in deionized water to create a synthetic “hydrothermal”
90 fluid at 500 ppm Si, similar to that used for previous cryogenic opal-A experiments (450 ppm Si¹⁸), and
91 also to concentrations found in hot spring fluids at Strokkur (476 ppm dissolved Si²⁹) and in Yellowstone
92 National Park (312-654 ppm)³⁰. This solution was buffered to pH 7.7 using HCl, and sterilised via 0.22 µm
93 filtering. Cultures of microorganisms were harvested by centrifugation (10,000× g for 15 minutes), washed
94 once in phosphate-buffered saline (130 mM NaCl, 1 mM NaH₂PO₄, 9 mM Na₂HPO₄, pH 7.7), and once in

95 sterile 500 ppm silica solution. Washed cells were resuspended in sterile 500 ppm silica solution that had
96 been preheated to 55 °C. An aliquot of sterile 500 ppm silica solution served as an experimental blank. All
97 experiments were frozen at -20 °C for 24 hours, after which they were thawed and prepared for analysis.

98

99 **2.3. Field sampling**

100 Fresh, naturally-formed cryogenic silica gels were collected from frozen hydrothermal fluid on the Strokkur
101 outflow apron, Geysir geothermal area, Iceland (64.312542 °N; 20.300367 °W) in January 2007 following
102 the protocol in Channing and Butler¹⁸. The Strokkur spring was the focus of sampling as the Geysir spring
103 has become much less active and is no longer continuously discharging fluid. Strokkur hydrothermal fluid
104 geochemistry was comparable to the experimental set-up, with alkaline (pH 8.5) fluids previously
105 characterised by 476 ppm dissolved Si²⁹. COA particles were extracted from these fresh gels as with the
106 experimental samples, with further volumes melted and evaporated within sterile petri dishes for visible -
107 shortwave infrared (Vis-SWIR), FTIR, and Raman spectroscopic analysis. Natural hydrothermal fluids and
108 their indigenous microbial communities were also collected for laboratory cyrosilicification. These were
109 collected aseptically from the Strokkur outflow in sterile bottles in February 2017, where the dissolved Si
110 content was 149 ppm (see below); considerably lower than previously measured²⁹. These fluids were then
111 frozen at -20°C in the laboratory, and the resulting COA precipitates extracted as described above.

112

113 **2.4. Determination of dissolved silica concentration**

114 Dissolved silica content of a fluid sample from the Strokkur discharge apron was determined by Inductively
115 Coupled Plasma Optical Emission Spectroscopy (ICP-OES) at the Open University using a Prodigy7
116 (Teledyne-Leeman) OES system at 250.960 nm. Samples were diluted by a factor of 20 prior to analysis.

117

118 **2.5. Optical and fluorescence microscopy**

119 For optical microscopy, aliquots of thawed experimental samples and thawed natural fluids were transferred
120 to glass slides and allowed to fully evaporate, before being gently rinsed with 0.22 µm-filtered MilliQ water
121 to remove salt crystals. These were imaged using a Keyence VHX 2000 digital microscope. For
122 fluorescence microscopy, aliquots of defrosted sample were stained with 1× SYBR Gold (Invitrogen),
123 incubated at room temperature in the dark for 15 minutes, and mounted on 25 mm diameter, 0.22 µm pore
124 size black polycarbonate filters. Samples were excited at 490 nm and imaged at 590 nm using an Amscope
125 T600 series epifluorescence microscope.

126

127 **2.6. Scanning Electron Microscope (SEM) Imaging**

128 Glass microscope slides used for optical microscopic analysis of experimental COA were subsequently
129 gold-coated for SEM analysis. Gold was chosen as coating material due to its suitability for secondary
130 electron (SE) topographic imaging. Experimental COA were imaged at 10 keV using the SE detector of a
131 Carl Zeiss SIGMA HD VP Field Emission SEM at the University of Edinburgh. COA produced from
132 natural Strokkur fluids were imaged at 5 keV using the SE detector of a Carl Zeiss SIGMA VP Field
133 Emission SEM. Aliquots of defrosted natural samples were placed on carbon pad stubs and gold-coated.
134 Naturally precipitated COA from Strokkur gels were imaged using the SE detector of a Phillips XL30
135 Environmental SEM at 20 keV and a working distance of 10 mm at the University of Cardiff.

136

137 **2.7. Vis-SWIR reflectance, FTIR, and Raman spectroscopy**

138 Aliquots of defrosted experimental COA (approximately 100 ml) were passed through a 0.22 µm filter to
139 recover COA particles, and rinsed with 0.22 µm-filtered MilliQ water to remove salt crystals. The resulting
140 powders were analysed alongside powdered (dry sieved <45 µm grain size) natural Strokkur COA at the

141 Planetary Spectrometer Facility, University of Winnipeg. Visible - SWIR (350 to 2500 nm) reflectance
142 spectra were acquired with an Analytical Spectral Devices FieldSpec Pro HR spectrometer in 1.4 nm steps
143 with a spectral resolution of 2 - 7 nm (internally resampled to 1 nm intervals) at a viewing geometry of
144 $i=30^\circ$ and $e=0^\circ$. A 150 W quartz-tungsten-halogen collimated light source provided incident lighting.
145 Spectra were measured relative to a 99% Labsphere Spectralon® standard and corrected for minor (<2%)
146 irregularities in its absolute reflectance. 500 spectra of the dark current, standard, and sample were acquired
147 and averaged. 1.25 to 25 μm (8000-400 cm^{-1})

148 Mid-infrared spectra were obtained using a Thermo Scientific Nicolet iS5 FTIR Spectrometer and an
149 Attenuated Total Reflectance (ATR) attachment equipped with a diamond crystal, housed in the Planetary
150 Spectroscopy Laboratory at Birkbeck, University of London. Reflectance measurements, published as
151 absorbance units, were obtained over a spectral range of 500 to 4000 cm^{-1} at a resolution of 4 cm^{-1} . A
152 diamond calibration standard was used and atmospheric water (H_2O) and carbon dioxide (CO_2) subtractions
153 made. No further processing of data (*e.g.*, smoothing or Fourier self-deconvolution) was used, to avoid the
154 introduction of artefacts. Band positions are reported simply as the observed maxima, rather than maxima
155 obtained from second derivations or from curve fits. Six analyses were taken of each powdered sample of
156 COA which were re-homogenised after each spectral acquisition to obtain an accurate spectral profile of
157 the material and its associated organic functional groups.

158 Raman spectra (175-4000 cm^{-1}) were collected at a resolution of $\sim 4 \text{ cm}^{-1}$ at 614 nm with a B&W Tek i-
159 Raman-532-S instrument using the automatic integration time function to maximise signal-noise-ratio.
160 Excitation was provided by a 532 nm $\sim 50 \text{ mW}$ solid state diode laser. Raman-scattered light was detected
161 by a Glacier™ T thermoelectrically cooled (14 °C) CCD detector. All measurements comprised a dark
162 current spectrum followed by sample measurement, using identical viewing geometry, integration time, and
163 number of averaged spectra. Raman-shift calibration was monitored through measurements of a polystyrene
164 standard.

165

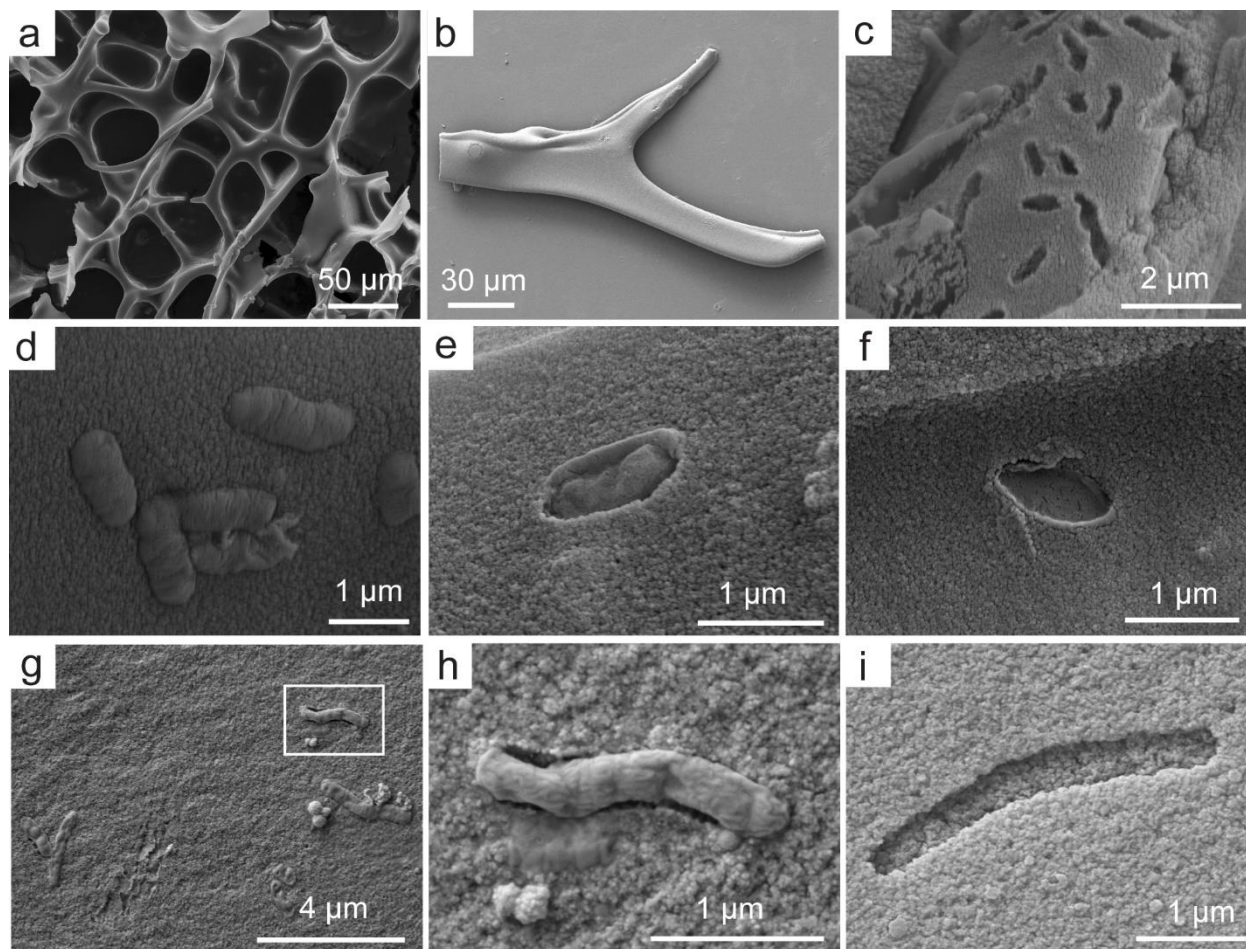
166

167 3. RESULTS

168 3.1. Cryogenic Opal-A particles

169 Natural COA particles (from the active Strokkur hot spring, Iceland) and experimental COA particles
170 produced both from natural Strokkur outflow fluids and synthetic high-silica laboratory fluids exhibit the
171 same distinctive particle morphologies identified previously by Channing and Butler¹⁸ and putative COA
172 particles observed in siliceous sediments in Iceland by Jones and Renaut²⁰. These included triple junctions
173 (Fig. 1b), terminal tear-drop and bulb morphologies, branched threads and sheets; particles produced via
174 the break-up of the COA lattice (Fig. 1a) following cryogelling¹⁸. Experimental COA particles produced
175 from both synthetic and natural fluids comprise colloidal silica microspheres and aggregates ~50 nm in
176 diameter.

177



178

179 **Figure 1.** SEM images of experimental and natural COA particles. (a) Intact experimental COA lattice. (b)

180 COA particle experimentally produced from natural Strokkur fluid, exhibiting triple-junction morphology.

181 (c) Experimental COA branch containing cell casts of *Rhodospseudomonas palustris* grown on Fe²⁺. (d)

182 Experimental COA sheet exhibiting fully encased cells of *R. palustris* grown on acetate. (e) Cell cast of *M.*

183 *thermophilus* on an experimental COA branch, containing cellular remnants. (f) ‘Empty’ cell cast of *M.*

184 *thermophilus* on an experimental COA branch. (g) Experimental COA produced from natural Strokkur fluid

185 exhibiting cellular structures within surface casts. Box indicates region magnified in panel (h), showing

186 cellular remnant within surface cast. (i) Cast with vibrio cell morphology hosted on COA sheet produced

187 from natural Strokkur fluid.

188

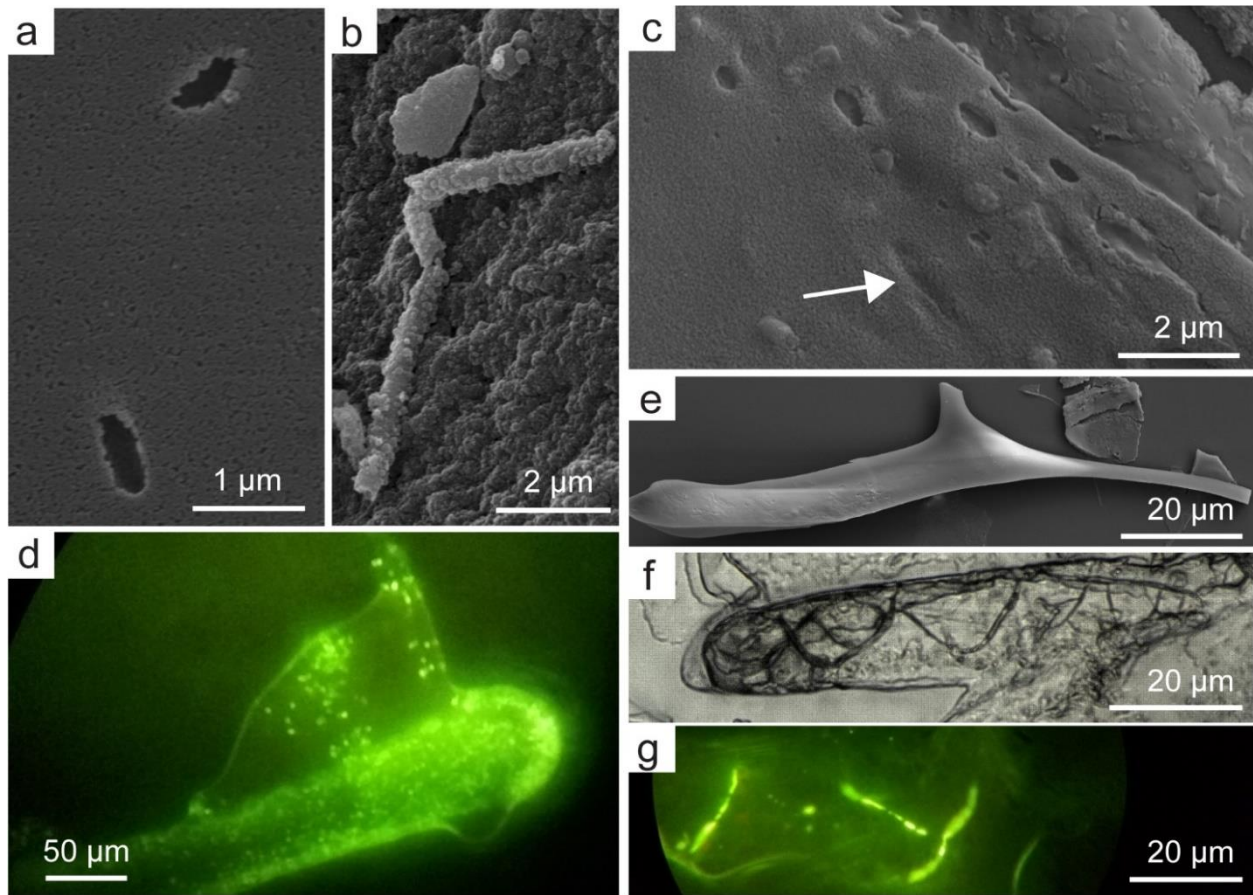
3.2. Microfossils in experimental and natural COA

189

190 Our microscopic observations reveal that microbial cells are incorporated into COA particles, becoming
191 completely or partially encased within the colloidal silica matrix. Multiple cell casts are observed on the
192 surface of COA particles and occur along branched threads, at terminal bulbs, and on sheet surfaces (Fig.
193 1c-i). External casts caused by single cell templating are produced by the photoferrotroph *R. palustris* (Fig.
194 1c, d) and the methanogenic archaeon *M. thermophilus* (Fig. 1e, f). In both cases, casts preserve their overall
195 cellular morphology. We also observe disintegrated remnants of *M. thermophilus* cells within casts (Fig.
196 1e) in close proximity to more typical ‘empty’ casts (Fig. 1f).

197 Experimental cryogenic silicification of natural fluids from the outflow apron at Strokkur, Iceland, also
198 resulted in the formation of biomorphic casts on the surface of COA particles (Fig. 1g-i). These include
199 casts containing cellular remnants, as observed with *M. thermophilus* (Fig. 1g, h), and empty casts, as
200 observed with *R. palustris* and *T. islandicus* (Fig. 1i). Empty biomorphic cast features are also observed
201 within natural COA particles extracted from gels at Strokkur (Fig. 2a). Other silicified biomorphic features
202 observed in this natural COA include rods or filaments encrusted with opal-A nanospheres in a manner not
203 observed in the experimental samples (Fig. 2b).

204 The mode of preservation differs between strains. In contrast to the well-preserved cellular morphologies
205 of *R. palustris* and *M. thermophilus*, casts formed by the sulfate-reducing bacterium *T. islandicus* show
206 significant morphological deformities, including shrunken or compressed cell shapes (Fig. 2c) that are
207 unlike the curved-rod ‘vibrio’ shape of the organisms in culture. Morphological evidence for secondary
208 opal-A crystallisation within casts is also present (Fig. 2c). These deformed cells are also observed on COA
209 particles using epi-fluorescence microscopy (Fig. 2d). Cell casts of the filamentous anoxygenic phototroph
210 *C. aurantiacus* are not observed on COA particle surfaces. Instead, the filamentous cells are incorporated
211 within the interior of COA particles, as revealed by optical and fluorescence microscopy (Fig. 2e-g).



212

213 **Figure 2.** SEM, light, and fluorescence microscope images of experimental and natural COA. (a)
 214 Biomorphic cell casts on the surface of a natural COA particle collected from Strokkur. (b) Possible
 215 microbial filament encrusted with opal-A microspheres from natural Strokkur COA. (c) Small and
 216 deformed cell casts of *T. islandicus*, with possible secondary infilling of earlier cast structures (arrow). (d)
 217 Fluorescence microscope image of *T. islandicus* COA bulb particle with similarly deformed cells
 218 distributed across the particle surface. (e-g) COA particles containing cells of *C. aurantiacus*. Note the
 219 absence of cellular microfossils at the surface of the large COA particle in SEM image (e), whilst filaments
 220 are clearly visible within transparent COA particles under both optical (f) and fluorescence microscopy (g).

221

222

223

224 3.3. Spectroscopic characterisation of natural and experimental COA

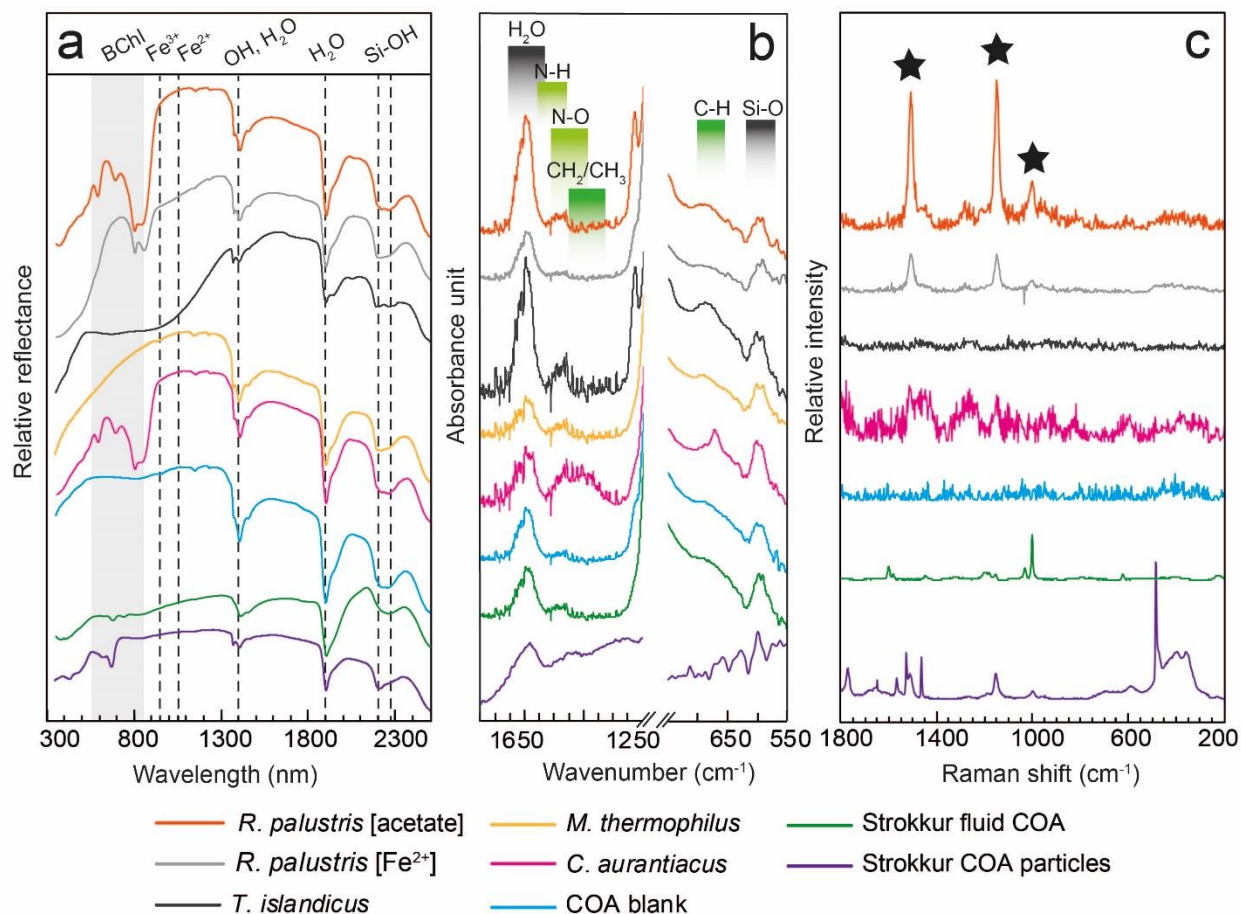
225 We observe characteristic SWIR spectral features for opal-A, as well as for organic molecules (visible,
226 FTIR, Raman), and inorganic and biomolecular signatures of microbial metabolism (Vis-SWIR) (Fig 3a-c
227 respectively).

228 3.3.1. Vis-SWIR reflectance

229 The SWIR reflectance spectra of all experimentally produced and natural COA particles show characteristic
230 absorption bands for hydrated opal-A, including hydration bands at 1.41 and 1.46 μm (interstitial or lattice-
231 bound water; Fig. 3a), water trapped within Si-cages (deep 1.9 μm absorption³¹), and the Si-OH double
232 absorption feature is observed at 2.21 and 2.26 μm ³¹. Rice et al.³¹ previously showed that hydrated silica
233 phases can be discriminated by comparing the depth and band minimum positions of SWIR hydration
234 bands. Applying band ratio analyses, we show that the experimental and natural COA spectra cluster as a
235 distinct population between the “opal, sinter, and synthetic” silica and “dehydrated sinter” fields³¹ (Fig. 4a).
236 Furthermore, natural Strokkur COA particles plot closer to more crystalline phases than the purely
237 experimental COA (Fig. 4b), and exhibit less hydration (Fig. 4c). Based on a comparison of the 1.41 and
238 1.91 μm band depths, experimentally-produced COA exhibits a range of water contents (Fig. 4c).

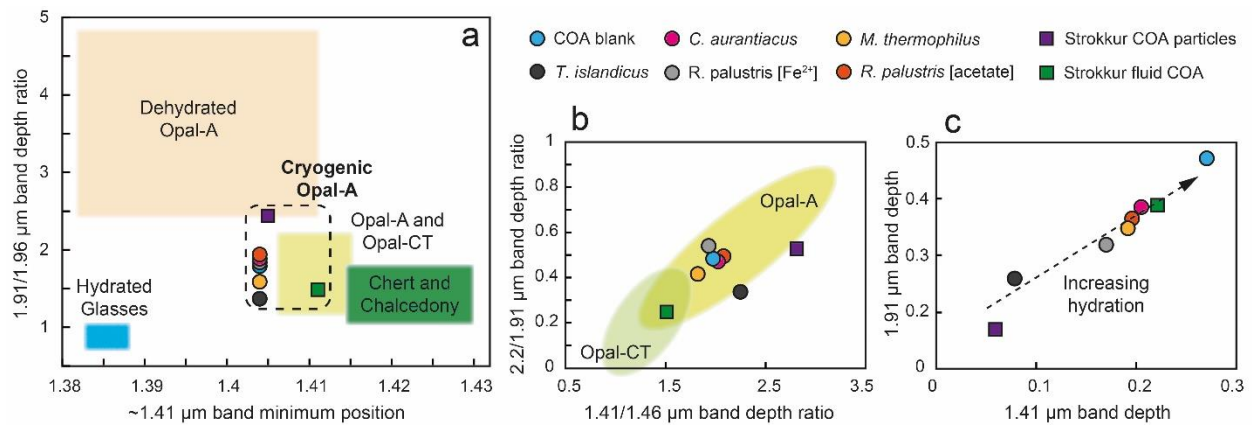
239 All experimental COA samples, including those produced from natural fluids, and the Strokkur COA
240 particulates, have a number of additional absorption features in the visible spectral region that are absent in
241 the experimental blank COA. Absorption bands of light-harvesting pigments bacteriochlorophyll *a* (590,
242 805 and 871 nm) and bacteriochlorophyll *c* (670 nm) are observed in COA containing *C. aurantiacus*, and
243 *R. palustris* (grown with acetate as the electron donor), and bacteriochlorophyll *c* peaks are also detectable
244 in COA experimentally produced from Strokkur fluids and the natural COA particles collected from
245 Strokkur (Fig. 3a). COA containing *R. palustris* (grown with Fe^{2+} as the electron donor) is characterised by
246 fewer bacteriochlorophyll bands (805 and 871 nm only), and instead exhibits a steep ferric absorption edge
247 between 400 – 700 nm, consistent with the presence of iron (oxyhydr)oxides. Finally, COA containing the

248 sulfate reducing bacterium *T. islandicus* shows a characteristic steep sulfur absorption between 350 – 550
 249 nm, and a broad Fe²⁺ absorption centred at 1000 nm, consistent with the presence of iron sulfide.



250
 251 **Figure 3.** Spectroscopic analysis of experimental and natural COA with band regions and major peaks
 252 identified. (a) visible – SWIR reflectance spectra showing absorption bands in the visible for
 253 bacteriochlorophyll pigments (BChl) and inorganic phases (dashed lines). (b) FTIR spectra showing
 254 absorption peaks relating to inorganic phases and organic functional groups. A large Si-O-Si asymmetric
 255 stretch feature at approx. 1051 cm⁻¹ in all samples has been removed for clarity. (c) Raman spectra with
 256 background fluorescence removed showing peaks for β-carotene (black star). Note *M. thermophilus* is not
 257 included for clarity due to large background fluorescence.

258



259

260 **Figure 4.** Band parameter plots from Rice *et al.*³¹ using SWIR reflectance bands at 1.91, 1.96, 1.41, 1.46,
 261 and 2.2 μm to characterise natural COA particles from Strokkur and laboratory-produced COA from natural
 262 Strokkur fluid (squares), and experimental COA with and without microorganisms (circles).

263

264 3.3.2. FTIR Spectroscopy

265 The FTIR spectra of both natural and experimental COA show absorption bands indicative of organic
 266 compounds, including an amine N-H bend between 1520 and 1600 cm⁻¹ for COA containing *R. palustris*
 267 (grown on acetate), *T. islandicus* and *C. aurantiacus*; alkane CH₂ or CH₃ bending vibrations centred at 1450
 268 cm⁻¹ exhibited prominently by *C. aurantiacus* COA; and an N-O asymmetric stretch centred at 1500 cm⁻¹
 269 for *M. thermophilus* COA and the natural COA particles collected from Strokkur (Fig. 3b). An alkene-
 270 related C-H bending vibration centred at 670 cm⁻¹ is also observed in COA containing *R. palustris* (grown
 271 on acetate), *T. islandicus*, and *C. aurantiacus*. Inorganic hydrated opal-A features at 1650 cm⁻¹ and 600 cm⁻¹
 272 are observed for all samples (Fig. 3b).

273

274 3.3.3. Raman Spectroscopy

275 Raman spectra from natural COA display a broad Si-O-Si peak between 350 – 500 cm⁻¹ that is absent in
 276 the experimental COA, but peaks for α-quartz (~465 cm⁻¹), meta-stable moganite (~502 cm⁻¹), or

277 paracrystalline opal-C ($\sim 777 \text{ cm}^{-1}$) and opal-CT (421 cm^{-1})^{32,33} are not observed. An additional, unidentified
278 peak at 490 cm^{-1} is also present in the natural sample. Beyond 800 cm^{-1} *R. palustris* COA and Strokkur
279 COA exhibit β -carotene peaks (Fig. 3a) at 1518, 1155, and 1003 cm^{-1} ³⁴. Pigment peaks are absent in *C.*
280 *aurantiacus* COA.

281

282 4. DISCUSSION

283 4.1. Cryosilicification of microorganisms

284 Our experiments demonstrate that cryogenic precipitation of opal-A can preserve morphological and
285 geochemical evidence of microorganisms in the resulting COA particles. As the fluid freezes, initial
286 nanoparticle nucleation ($\geq 8 \text{ nm}^{35}$) is preceded by rapid COA aggregation between ice crystals as
287 temperature drops below 0° C , trapping microorganisms. Thus, the cryogenic silicification of
288 microorganisms differs from silicification under non-freezing conditions where gradual nanoparticle
289 growth and sinter sedimentation dominate³⁶. Similar biomorphic microfossils were observed in the pure-
290 strain experimental COA, experimental COA produced from natural Strokkur fluids and in natural COA
291 particles collected from Strokkur (Fig. 1, 2), providing strong evidence that the encapsulation of
292 microorganisms in this manner is active in nature. Furthermore, the production of COA particles from
293 natural Strokkur fluids, despite a lower initial Si content compared to the experimental fluids (149 ppm vs.
294 500 ppm), demonstrates that this process occurs across a range of silica concentrations. Observation of cell
295 remnants *in situ* within casts produced by *M. thermophilus* and in COA produced from natural Strokkur
296 fluids (Fig. 1e, g, h) suggests large cellular structures such as membranes and/or cell walls can be captured
297 within COA surface casts and ultimately silicified.

298 By experimenting with model microbial strains we also show that the mechanics of microbial
299 cryosilicification can vary, and in the first instance appear to be controlled by cell morphology. Strains with
300 curved-rod (*T. islandicus*, *R. palustris*) or irregular coccoid (*M. thermophilus*) cell morphology produce

301 casts on the surface of COA particles, suggesting individual cells are ‘sandwiched’ between the growing
302 ice crystal face and increasing volume of COA aggregates. Observing these features in COA produced from
303 natural fluids (Fig. 1g-i) demonstrates that the trapping of cells in this manner is active in nature. However,
304 the absence of cell casts for *C. aurantiacus* on COA particle surfaces shows that surficial casting is not the
305 sole mechanism of preservation. Instead, filamentous bacteria (e.g. *C. aurantiacus*) may only be preserved
306 when entirely encased within COA particles (Fig. 2e-g). The absence of bacteriochlorophyll or β -carotene
307 peaks in the *C. aurantiacus* COA Raman spectrum (Fig. 3) is consistent with this, whereby pigments
308 trapped within the translucent COA matrix are detectable using reflectance spectroscopy, but not via surface
309 excitation and Raman scattering.

310 Functional groups on the surface of microbial cells can act as nucleation sites for opal-A under non-freezing
311 precipitation³⁷, despite this process being inefficient when compared with spontaneous (abiotic) silica
312 growth³⁸. *C. aurantiacus* is unique amongst our experimental strains in that it grows in sheathed filamentous
313 colonies, and the cell wall stains Gram-negative but carries Gram-positive traits such as a single lipid layer
314 and S-layer protein³⁹. Whether these characteristics contribute to active silica nucleation is unclear, but our
315 data suggest that *C. aurantiacus* is more efficient at initiating COA precipitation around its entire cell mass,
316 relative to the other microorganisms investigated. The morphologies of our experimental microfossils are
317 otherwise consistent with their corresponding microbial strains, with the sole exception of casts produced
318 by *T. islandicus*, which underwent physical deformation during the cryogelling process (Fig. 2c). The
319 identification by epi-fluorescence microscopy of numerous DNA-bearing cells of a similar size, shape and
320 distribution to the *T. islandicus* casts observed by SEM attests to their biogenicity (Fig. 2d). Finally, all
321 experimental COA fossilising microorganisms shows a shift in the 1.91/1.96 μm SWIR ratio (both positive
322 and negative - Fig. 4a), with no corresponding change to the 1.41 μm band minima position. As the 1.96
323 band is attributable to the presence of free water molecules³¹, this characteristic shift, as well as the broad
324 spread in water content revealed by comparing the 1.41 and 1.91 μm band depths (Fig. 4c) can be explained
325 by the retention of water molecules to differing degrees by captured microorganisms.

326

327 **4.2. Cryosilicification vs. Non-cryogenic Silicification**

328 By documenting microbial silicification under fully cryogenic conditions, these data provide new insights
329 relating to the preservation of biological activity in hydrothermal systems that experience freezing
330 temperatures. For example, our results contrast with previous investigations into microbial silicification at
331 low temperatures. Westall et al.⁴⁰ showed that after a week at 4 °C, many microorganisms (including
332 diatoms, fungi and bacteria) were not silicified, and even after four weeks several bacterial strains remained
333 unsilicified. The precipitation of opal-A on and around microbes in this experiment was characterised by
334 the gradual growth of silica sheaths surrounding cells, and the formation of silica spheroids of up to 2 µm
335 in diameter⁴⁰. Evidence for similar silicification mechanisms were also observed at low temperatures in
336 deep sea environments⁴¹. These low-temperature studies show similarity to mechanisms described at higher
337 temperatures, both in nature³ and in the laboratory³³, where gradual sedimentation of large spheroids and
338 the precipitation of cell sheaths dominate the silicification processes. However, in the current study, small
339 (~50 nm; Fig. 1) COA spheroids rapidly formed surface casts or entirely encased microorganisms. Our
340 experiments therefore show that the formation of ice crystals distinguishes this cryogenic process from non-
341 freezing silicification, even when silicification is occurring at low temperatures. Specifically, the formation
342 of concentrated siliceous brines is necessary to drive the precipitation of COA and subsequent capture of
343 microorganisms.

344 In nature, it is likely that both non-freezing and cryogenic silicification processes are occurring
345 simultaneously. Natural particles with cryogenic morphologies from Strokkur, Iceland, exhibited
346 filamentous biogenic structures encrusted in larger opal-A nanospheres in a manner akin to those observed
347 in previous non-freezing silicification studies^{40,41} (Fig. 2b), as well as the smaller COA nanospheres and
348 biomorphic casts typical of experimental COA (Fig. 2a). Silicified microorganisms previously reported in
349 spatial association with natural COA particles in Iceland²⁰ were encrusted with relatively large spheroids
350 (~2 µm²⁰), whilst the COA particles themselves lacked visible cell casts. Viewed in the context of our

351 observations, these features are suggestive of non-freezing silicification and imply that these
352 microorganisms were silicified under different conditions from the formation of the COA.

353 On Earth, mid-to-high-latitude and high-altitude hydrothermal systems can experience prolonged sub-zero
354 °C air temperatures^{20,21}, promoting prolific COA formation. In such localities, cryogenic and non-freezing
355 silicification mineralise different portions of the microbial consortia, whereby the latter predominantly
356 captures biofilms, streamer communities and other benthic organisms⁴². Conversely, cryogenic
357 silicification is likely to more efficiently capture the planktic microorganisms present in the fluid-phase,
358 where ice-formation primarily occurs. Unconsolidated COA particles can become cemented by summer-
359 time sinter development, with the distinctive shape of COA particles identifiable even within reworked
360 sediments²⁰, but in environments with little to no summertime sinter growth, COA particles are free to be
361 exported when the ice matrix thaws¹⁸. Under these circumstances, the retention of cells within COA raises
362 questions about whether cells can remain viable following rapid cryosilicification, as has been observed for
363 organisms under non-cryogenic conditions⁴³. If so, dispersal of microorganisms within COA particles may
364 have ecological significance in hydrothermal settings.

365

366 **4.3. Relevance to Mars and icy moons**

367 The recent discovery of both colloidal silica and H₂ being erupted from within Enceladus^{14,15} means the
368 subsurface environment could be habitable for simple methanogenic organisms, and that such organisms
369 might be cryogenically silicified in a similar manner to that shown here. Such processes should be further
370 investigated with specific relevance to future surface exploration of Enceladus and other icy moons, such
371 as Europa. Closer to home, one of the shortlisted landing sites for NASA's Mars 2020 rover (Columbia
372 Hills) includes relic hydrothermal systems, and confirmed deposits of opal-A¹¹. As vast areas of the Martian
373 surface have experienced persistent freezing temperatures for much of its history^{44,45}, it is likely that the
374 surface discharge of subsurface silica-rich hydrothermal fluids would lead to COA precipitation, trapping

375 some portion of any putative subsurface Martian microbiota within these COA deposits. Moreover,
376 upcoming Mars surface missions will be equipped with SWIR reflectance spectroscopy (NASA Mars 2020
377 and ESA ExoMars 2020). We show here that COA deposits would feasibly be identifiable and
378 distinguishable from other amorphous or hydrated silica phases using such instrumentation (Fig. 4), with a
379 broad range of hydration also observed across the experimental and natural samples (Fig. 4c). However,
380 these spectral features are likely to become less pronounced with prolonged exposure to the desiccating
381 atmospheric conditions on Mars. Likewise, the presence of a broad Raman peak between 300 – 500 cm⁻¹ in
382 the natural COA particles (Fig. 3a) suggests that freshly-precipitated, unstable COA will eventually develop
383 into more ordered states where energy is available to drive this kinetic process, consistent with the
384 development of other silica sinter deposits⁴⁶.

385

386 **4.4. Spectral detection of biosignatures**

387 Consistent with previous works⁴⁷, the spectral detection of non-pigmented biomass in geological substrates
388 remains challenging. The most prominent biomolecular features in the vis-SWIR and Raman spectra are
389 photosynthetic pigments (Fig. 3a), and organic molecule-related absorption features detected in FTIR
390 spectra are minor in comparison to silica-related features, despite the considerable biomass observed with
391 microscopic methods in the experimental samples (Fig. 2d, g). Whilst specialised pigments such as
392 bacteriochlorophyll are unlikely to exist beyond Earth, they serve to demonstrate the capacity of COA
393 formation in the capture of functional biological molecules, and the utility of combined Raman and Vis-
394 SWIR reflectance spectroscopy in the characterisation of such deposits on extraterrestrial surfaces such as
395 Mars and icy moons. Recent work by Dos Santos et al.⁴⁸ revealed variation in the UV-shielding effects of
396 minerals on amino acids, while opal-A sinters can be effective absorbers of UV-C and UV-B within the top
397 1 mm of substrate⁴⁹. Furthermore, previous studies of biomolecule preservation⁵⁰ have indicated that, over
398 geological time, the observation of amide absorption bands within rocks and minerals decreases, whereas
399 hydrocarbons such as those detected by FTIR here are more persistent. The ability of COA to effectively

400 shield biomolecules, or any other captured organics, from other damaging forms of surface radiation and
401 oxidative reactions over representatively long time periods remains to be determined. Similarly, the
402 longevity of COA deposits and cryogenically-generated microfossils in the terrestrial rock record is
403 unknown. However this study demonstrates that investigations of this sort are now required, as they would
404 further define the importance of COA as target phase for extraterrestrial exploration. Likewise, quantifying
405 the effects of different freezing rates, initial fluid temperatures, and the presence of other solutes on the
406 efficiency of cryogenic silicification should constitute future studies.

407

408 **Acknowledgements**

409 This work was supported by The Carnegie Trust (REF: 70335), The Leverhulme Trust (REF: RPG-2016-
410 153), and a Royal Society of Edinburgh research fellowship to CRC. EAC thanks the Canadian Space
411 Agency, the Natural Sciences and Engineering Research Council of Canada, the Canada Foundation for
412 Innovation, the University of Winnipeg, and the Manitoba Research Innovations Fund for supporting the
413 University of Winnipeg's Planetary Spectrophotometer Facility. The authors thank the National Energy
414 Authority (Orkustofnun) in Iceland for a research permit allowing microbiology research to be conducted
415 at Geysir, and the Iceland Institute of Natural History for permission to export the samples. ICP-OES data
416 from an Icelandic fluid sample was acquired by Timothy Barton and Nisha Ramkissoon of the Open
417 University.

418

419 **Author contributions**

420 MGFP led and conducted all experimental work, collection of all imaging data for experimental samples,
421 interpretation of data, and authorship of the manuscript. CRC led the study, contributed to the collection
422 and interpretation of data, and co-authored the manuscript. AC collected natural cryogenic opal-A samples
423 from Iceland, associated SEM data, and contributed to the interpretation of data. DA and EAC collected

424 vis-SWIR and Raman spectroscopic data and contributed to their interpretation. LJP collected FTIR
425 spectroscopic data and contributed to their interpretation.

426 **Competing financial interests:** All authors declare that they do not have any competing financial interests.

427

428 5. REFERENCES

429 1. Cady, S. L. & Farmer, J. D. in *Evolution of hydrothermal ecosystems on Earth (and Mars?)* (eds.
430 Bock, G. R. & Goode, J. A.) 150–173 (Wiley, 1996).

431 2. Westall, F. *et al.* Biosignatures on Mars: What, Where, and How? Implications for the Search for
432 Martian Life. *Astrobiology* **15**, 998–1029 (2015).

433 3. Jones, B., Renaut, R. & Rosen, M. Taphonomy of Silicified Filamentous Microbes in Modern
434 Geothermal Sinters: Implications for Identification. *Palaios* **16**, 580–592 (2001).

435 4. Preston, L. J., Benedix, G. K., Genge, M. J. & Sephton, M. A. A multidisciplinary study of silica
436 sinter deposits with applications to silica identification and detection of fossil life on Mars. *Icarus*
437 **198**, 331–350 (2008).

438 5. Grasby, S. E., Bezys, R. & Beauchamp, B. Silica Chimneys Formed by Low-Temperature Brine
439 Spring Discharge. *Astrobiology* **9**, 931–941 (2009).

440 6. Djokic, T., Kranendonk, M. J. Van, Campbell, K. A., Walter, M. R. & Ward, C. R. Earliest signs of
441 life on land preserved in ca. 3.5 Ga hot spring deposits. *Nat. Commun.* **8**, (2017).

442 7. Ruff, S. W. & Farmer, J. D. Silica deposits on Mars with features resembling hot spring
443 biosignatures at El Tatio in Chile. *Nat. Commun.* **7**, 1–10 (2016).

444 8. Milliken, R. E. *et al.* Opaline silica in young deposits on Mars. *Geology* **36**, 847–850 (2008).

445 9. Squyres, S. W. *et al.* Detection of Silica-Rich Deposits on Mars. *Science* (80-.). **320**, 1063–1067

- 446 (2008).
- 447 10. Skok, J. R., Mustard, J. F., Ehlmann, B. L., Milliken, R. E. & Murchie, S. L. Silica deposits in the
448 Nili Patera caldera on the Syrtis Major volcanic complex on Mars. *Nat. Geosci.* **3**, 838–841 (2010).
- 449 11. Ruff, S. W. *et al.* Characteristics, distribution, origin, and significance of opaline silica observed by
450 the Spirit rover in Gusev crater, Mars. *J. Geophys. Res. E Planets* **116**, (2011).
- 451 12. Rice, M. S. *et al.* Silica-rich deposits and hydrated minerals at Gusev Crater, Mars: Vis-NIR spectral
452 characterization and regional mapping. *Icarus* **205**, 375–395 (2009).
- 453 13. Farley, K. A. & Williford, K. H. *Report on the outcomes of the third Mars 2020 Landing Site*
454 *Workshop.* (2017).
- 455 14. Hsu, H.-W. *et al.* Ongoing hydrothermal activities within Enceladus. *Nature* **519**, 207–210 (2015).
- 456 15. Waite, J. H. *et al.* Cassini finds molecular hydrogen in the Enceladus plume: Evidence for
457 hydrothermal processes. *Science (80-.).* **356**, 155–159 (2017).
- 458 16. Taubner, R.-S. *et al.* Biological methane production under putative Enceladus-like conditions. *Nat.*
459 *Commun.* **9**, (2018).
- 460 17. Carr, M. H. & Head, J. W. Geologic history of Mars. *Earth Planet. Sci. Lett.* **294**, 185–203 (2010).
- 461 18. Channing, A. & Butler, I. B. Cryogenic opal-A deposition from Yellowstone hot springs. *Earth*
462 *Planet. Sci. Lett.* **257**, 121–131 (2007).
- 463 19. Mader, H. M., Pettitt, M. E., Wadham, J. L., Wolff, E. W. & Parkes, R. J. Subsurface ice as a
464 microbial habitat. *Geology* **34**, 169–172 (2006).
- 465 20. Jones, B. & Renaut, R. W. Impact of Seasonal Changes on the Formation and Accumulation of Soft
466 Siliceous Sediments on the Discharge Apron of Geysir, Iceland. *J. Sediment. Res.* **80**, 17–35 (2010).
- 467 21. Nicolau, C., Reich, M. & Lynne, B. Physico-chemical and environmental controls on siliceous sinter

- 468 formation at the high-altitude El Tatio geothermal field, Chile. *J. Volcanol. Geotherm. Res.* **282**, 60–
469 76 (2014).
- 470 22. Skirinisdottir, G., et al. Influence of sulfide and temperature on species composition and community
471 structure of hot spring microbial mats. *Appl. Environ. Microbiol.* **66**, 2835-2841 (2000)
- 472 23. Hedlund, B. P., Dodsworth, J. A., Cole, J. K. & Panosyan, H. H. An integrated study reveals diverse
473 methanogens, *Thaumarchaeota* and yet-uncultivated archaeal lineages in Armenian hot springs.
474 *Antonie van Leeuwenhoek* **104**, 71-82 (2013)
- 475 24. Akimov, N., Podosokorskaya, O. A., Shlyapnikov, M. G. & Gal, V. F. Dominant phylotypes in the
476 16S rRNA gene clone libraries from bacterial mats of the Uzon Caldera (Kamchatka, Russia)
477 hydrothermal springs. *Microbiology* **82**, 721-727 (2013)
- 478 25. Sonne-Hansen, J. & Ahring, B. K. *Thermodesulfobacterium hveragerdense* sp. nov., and
479 *Thermodesulfovibrio islandicus* sp. nov., two thermophilic sulfate reducing bacteria isolated from a
480 Icelandic hot spring. *Syst. Appl. Microbiol.* **22**, 559–564 (1999).
- 481 26. Rivard, C. J. & Smith, P. H. Isolation and characterization of a thermophilic marine methanogenic
482 bacterium, *Methanogenium thermophilicum* sp. nov. *Int. J. Syst. Bacteriol.* **32**, 430–436 (1982).
- 483 27. Pierson, B. K. & Castenholz, R. W. A phototrophic gliding filamentous bacterium of hot springs,
484 *Chloroflexus aurantiacus*, gen. and sp. nov. *Arch. Microbiol.* **100**, 5–24 (1974).
- 485 28. Jiao, Y., Kappler, A., Croal, L. R., Newman, K. & Newman, D. K. Isolation and characterization of
486 a genetically tractable photoautotrophic Fe (II) -oxidizing bacterium , *Rhodopseudomonas palustris*
487 strain TIE-1. *Appl. Environ. Microbiol.* **71**, 4487–4496 (2005).
- 488 29. Konhauser, K. O. & Ferris, F. G. Diversity of iron and silica precipitation by microbial mats in
489 hydrothermal waters, Iceland: Implications for Precambrian iron formations. *Geology* **24**, 323–326
490 (1996).

- 491 30. Fournier, R. O. Geochemistry and dynamics of the Yellowstone National Park hydrothermal system.
492 *Annu. Rev. Earth Planet. Sci.* **17**, 13–53 (1989).
- 493 31. Rice, M. S. *et al.* Reflectance spectra diversity of silica-rich materials: Sensitivity to environment
494 and implications for detections on Mars. *Icarus* **223**, 499–533 (2013).
- 495 32. Kingma, K. J. & Hemley, R. J. Raman spectroscopic study of microcrystalline silica. *Am. Mineral.*
496 **79**, 269–273 (1994).
- 497 33. Lynne, B. Y., Campbell, K. A., Moore, J. N. & Browne, P. R. L. Diagenesis of 1900-year-old
498 siliceous sinter (opal-A to quartz) at Opal Mound, Roosevelt Hot Springs. *Sediment. Geol.* **179**, 249–
499 278 (2005).
- 500 34. Marshall, C. P. & Marshall, A. O. The potential of Raman spectroscopy for the analysis of
501 diagenetically transformed carotenoids. *Philos. Trans. R. Soc. A* **368**, 3137–3144 (2010).
- 502 35. Tobler, D. J., Shaw, S. & Benning, L. G. Quantification of initial steps of nucleation and growth of
503 silica nanoparticles: An in-situ SAXS and DLS study. *Geochim. Cosmochim. Acta* **73**, 5377–5393
504 (2009).
- 505 36. Orange, F. O., Lalonde, S. V & Konhauser, K. O. Experimental Simulation of Evaporation-Driven
506 Silica Sinter Formation and Microbial Silicification in Hot Spring Systems. *Astrobiology* **13**, 163–
507 176 (2013).
- 508 37. Konhauser, K. O., Jones, B., Phoenix, V. R., Ferris, G. & Renaut, R. W. The Microbial Role in Hot
509 Spring Silicification. *AMBIO A J. Hum. Environ.* **33**, 552–558 (2004).
- 510 38. Yee, N., Phoenix, V. R., Konhauser, K. O., Benning, L. G. & Ferris, F. G. The effect of
511 cyanobacteria on silica precipitation at neutral pH: Implications for bacterial silicification in
512 geothermal hot springs. *Chem. Geol.* **199**, 83–90 (2003).
- 513 39. Pierson, B. K. & Castenholz, R. W. in *Bergey's Manual of Systematics of Archaea and Bacteria* 1–

- 514 16 (John Wiley & Sons, Inc., in association with Bergey's Manual Trust, 2015).
515 doi:10.1002/9781118960608.gbm00380.
- 516 40. Westall, F., Boni, L. & Guerzoni, E. The experimental silicification of microorganisms.
517 *Palaeontology* **38**, 495–528 (1995).
- 518 41. Monty, C. L. V., Westall, F. & van der Gaast, S. Diagenesis of siliceous particles in subantarctic
519 sediments, hole 699A: Possible microbial mediation. *Proc. Ocean Drill. Program, Sci. Results* **114**,
520 685–710 (1991).
- 521 42. Schultze-Lam, S., Ferris, F. G., Konhauser, K. O. & Wiese, R. G. In situ silicification of an Icelandic
522 hot spring microbial mat: implications for microfossil formation. *Can. J. Earth Sci.* **32**, 2021–2026
523 (1995).
- 524 43. Phoenix, V. R., Adams, D. G. & Konhauser, K. O. Cyanobacterial viability during hydrothermal
525 biomineralisation. *Chem. Geol.* **169**, 329–338 (2000).
- 526 44. Fairén, A. G. A cold and wet Mars. *Icarus* **208**, 165–175 (2010).
- 527 45. Wordsworth, R. D., Kerber, L., Pierrehumbert, R. T., Forget, F. & Head, J. W. Comparison of 'warm
528 and wet' and 'cold and icy' scenarios for early Mars in a 3-D climate model. *J. Geophys. Res.*
529 *Planets* **120**, 1201–1219 (2015).
- 530 46. Herdianita, N. R., Browne, P. R. L., Rodgers, K. A. & Campbell, K. A. Mineralogical and textural
531 changes accompanying ageing of silica sinter. *Miner. Depos.* **35**, 48–62 (2000).
- 532 47. Gaboyer, F. *et al.* Mineralization and Preservation of an extremotolerant Bacterium Isolated from
533 an Early Mars Analog Environment. *Sci. Rep.* **7**, (2017).
- 534 48. Dos Santos, R., Patel, M., Cuadros, J. & Martins, Z. Influence of mineralogy on the preservation of
535 amino acids under simulated Mars conditions. *Icarus* **277**, 342–353 (2016).

- 536 49. Phoenix, V. R., Bennett, P. C., Engel, A. S., Tyler, S. W. & Ferris, F. G. Chilean high-altitude hot-
537 spring sinters: a model system for UV screening mechanisms by early Precambrian cyanobacteria.
538 *Geobiology* **4**, 15–28 (2006).
- 539 50. Preston, L. J. *et al.* The preservation and degradation of filamentous bacteria and biomolecules
540 within iron oxide deposits at Rio Tinto, Spain. *Geobiology* **9**, 233–249 (2011).